analytical chemistry

pubs.acs.org/ac

Article

# Quasi-One-Dimensional Generator-Collector Electrochemistry in Nanochannels

Zinaida A. Kostiuchenko and Serge G. Lemay*

Cite This: *Anal. Chem.* 2020, 92, 2847−2852

Read Online

ACCESS | Metrics & More | Article Recommendations | Supporting Information

**ABSTRACT:** Mass transport in fluidic channels under conditions of pressure-driven flow is controlled by a combination of convection and diffusion. For electrochemical measurements the height of a channel is typically of the same order of magnitude as the electrode dimensions, resulting in complex two- or three-dimensional concentration distributions. Electrochemical nanofluidic devices, however, can have such a low height-to-length ratio that they can effectively be considered as one-dimensional. This greatly simplifies the modeling and quantitative interpretation of analytical measurements. Here we study mass transport in nanochannels using electrodes in a generator-collector configuration. The flux of redox molecules is monitored amperometrically. We observe the transition from diffusion-dominated to convection-dominated transport by varying both the flow velocity and the distance between the electrodes. These results are described quantitatively by the one-dimensional Nernst−Planck equation for mass transport over the full range of experimentally accessible parameters.

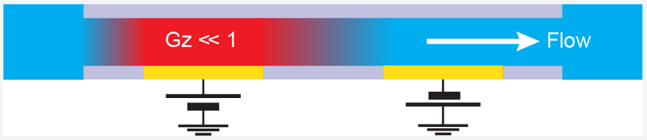


In an electrochemical generator-collector measurement, species that are reduced or oxidized at a generator electrode are converted back to their original state at a collector electrode. An early illustration of this principle was introduced in 1959 and consisted of a rotating disk electrode surrounded by a concentric ring electrode, the two electrodes being separated by a dielectric layer.[1] Double electrodes in channel flow, consisting of two closely spaced flat electrodes embedded into the wall of a channel through which the sample flowed, appeared shortly afterward.[2] More recently, double electrodes in a channel were applied for the study of electrode dissolution processes,[3−6] mechanisms and kinetics of electrochemical reactions[7−13] and *in situ* velocimetry.[14−18] Understanding mass transport in these systems became an important issue from the beginning, demanding complex calculations to account for complex geometries and different transport mechanisms.[19−25] Further miniaturization resulted in microchannel structures that allowed simplification to a two-dimensional description because mass transport becomes essentially uniform in the third dimension. However, the interplay between diffusion and convection, where changes in flow velocity alter the concentration profile in two dimensions, can remain highly nontrivial to quantify.

Here we employ nanofluidic devices in which the ratio between channel height and electrode length effectively removes one more dimension. This significantly simplifies the description of mass transport to the one-dimensional Nernst−Planck equation. To our knowledge, no electrochemical double-electrode systems with one-dimensional concentration distributions in the full accessible fluid velocity range were introduced previously.

Three main parameters characterize the nature of the analyte transport inside the nanochannel. The first parameter is the transverse Peclet number, $Pe^t$, which indicates how efficient diffusion is at mixing molecules across the height of the nanochannel during advective transport. Its value is given by $Pe^t = vh/D$, where $D$ is the diffusion coefficient of redox active species, $v$ is the average flow velocity and $h$ is the height of the channel. Typical values of the parameters, $h$ = 100 nm, $D$ = $10^{-9}$ $m^2/s$ and $v$ = 1000 $\mu$m/s yield $Pe^t$ = 0.1. This indicates that the diffusion across the nanochannel happens sufficiently fast that the parabolic shape of the laminar Poisseuille flow profile is effectively sampled. We can thus consider that all molecules are advected with the same velocity along the channel.

A second parameter, the Graetz number ($Gz$), also compares diffusion perpendicular to the nanochannel with convection along it, but at the length scales characteristic for each direction. It is the ratio of the time for a redox molecule to diffuse vertically across the nanochannel to the advection time along a length $L$. Here the importance of the high ratio between electrode length and channel height comes to light. For $L$ = 10 $\mu$m and $v$ = 1000 $\mu$m/s, which is maximum velocity used in the experiment, $Gz = Pe^t h/L = 10^{-3}$. This indicates that in a nanochannel the vertical mass transport equilibrates essentially instantly on the time and length scales over which longitudinal transport takes place for typical dimensions and all

**Received:** November 28, 2019
**Accepted:** January 14, 2020
**Published:** January 14, 2020




https://dx.doi.org/10.1021/acs.analchem.9b05396
*Anal. Chem.* 2020, 92, 2847−2852

(realistic) flow rates. This is a crucial difference with microchannels, where flow alters the concentration profile in both longitudinal and perpendicular directions, as sketched in Figure 1. A low value of $Gz$ allows utilizing a one-dimensional

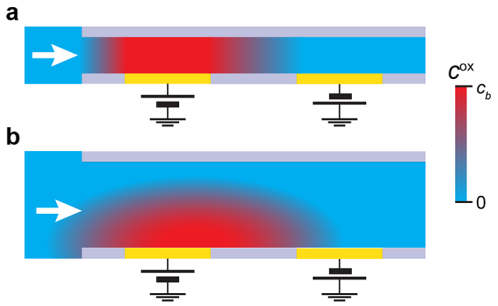


**Figure 1.** Qualitative representation of concentration profiles under high flow rate conditions for (a) a nanochannel and (b) a microchannel. The white arrows represent the flow direction.

description for calculating redox species concentrations in the nanochannel, in contrast with microchannels where two dimensions must be considered.

The third parameter is of particular interest here as it characterizes the dominant form of interaction between the electrodes. Transport of analyte along the nanochannel involves both diffusion and convection caused by externally applied pressure. The longitudinal Peclet number, $Pe^{l} = vs/D$ (where $s$ is the spacing between the electrodes), describes the ratio of each component's contribution. When it is much lower than one, diffusion dominates over convection, while in the opposite limit transport along the channel is controlled by convection. In the experiments described herein we will access both of these regimes by controlling $v$ and $s$.

## MATERIALS AND METHODS

A sketch of our fluidic system is depicted in Figure 2a. It consists of a nanochannel with two electrodes embedded in its floor and a microchannel connected in parallel. While the measurements take place in the nanochannel, the presence of the microchannel facilitates fluid handling and allows replacing

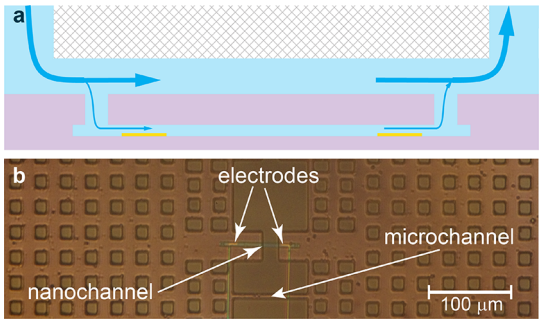


**Figure 2.** (a) Schematic side view of the measurement system consisting of a $SiO_2$ nanochannel (pink) with embedded Pt electrodes (yellow) and a PDMS microchannel in parallel (white). Not drawn to scale: in the experiment the nanochannel length and the microchannel height were ~1000 and 33 times the nanochannel height, respectively. (b) Micrograph of a chip with a nanochannel and electrodes, as well as the PDMS microstructure bonded on top. The structures are imaged through the PDMS. The regularly spaced squares are support pillars for the large access channels that lead to external fluidic connections.

solutions in reasonable time. We call 'upstream' and 'downstream' the electrodes closest to the fluid inlet and outlet, respectively.

**Nanofluidic Device.** The nanochannel was fabricated in a manner analogous to a previously reported process for nanogap electrodes.[26] In short, a Si wafer with thermally grown 500 nm $SiO_2$ was taken as substrate. The 20 nm thick Pt electrodes and connecting wires were defined by photolithography using photoresist OIR 907-12 and deposited by e-beam evaporation. These electrodes had a length of 11 $\mu$m and were separated by 2, 5, or 50 $\mu$m. A Cr sacrificial layer 86 $\mu$m long, 5 $\mu$m wide, and 90 nm high was then patterned on top of the electrodes with the same techniques to define the shape of the nanochannel. The entire wafer including the metal structures was then passivated with a layer of $SiO_2$ using chemical vapor deposition to isolate the leading wires from the analyte. Finally, two holes were created through the dielectric layer by reactive plasma etching to provide access to the Cr sacrificial layer. Immediately prior to an experiment, the Cr was removed with a wet etchant (Selectipur, BASF) to release the nanochannel. This procedure took 40−80 min, following which the chip was flushed with water and dried in a flow of nitrogen.

**Microfluidic Channels.** A microfluidic structure was formed on the bottom of a block of polydimethysiloxane (PDMS) using a lithographically patterned SU-8 mold. This structure consisted of two microchannels, each 90 $\mu$m long, 5 $\mu$m wide, and 3 $\mu$m high, connecting two large reservoirs. Punching holes through the PDMS in the regions of the large reservoirs allowed inserting polytetrafluoroethylene (PTFE) microtubes for external connections. To create the micro/nanochannel assembly, each chip was placed inside a plasma cleaner following release of the nanochannel together with a PDMS block and treated with oxygen plasma at 1 mbar for 70 s to activate the surfaces for bonding. The microstructure on the PDMS block was then aligned with the nanogap device under a microscope and pressed against the chip. The assembled system was thereafter placed in an oven at 70 °C for 15−20 min to enhance bonding strength. After this, we placed the chip with its assembled microfluidic structure in a custom probe station and inserted microtubes into the inlet and outlet holes. An image of the complete structure is shown in Figure 2b.

**Flow control.** The inlet of the device was connected to a 500 $\mu$L ILS microsyringe driven by a syringe pump (Pump 11 Pico Plus Elite) and the outlet to a reservoir with a Ag/AgCl reference electrode (BASi, MF 2079, RE-5B) immersed in it. According to Poiseuille's law, the pressure difference $\Delta p$ caused by a flow rate $Q_{total}$ in such a system is defined as $\Delta p = Q_{total}R_{total}$, where $R_{total}$ is the total hydraulic resistance. For a channel with a rectangular cross-section, an estimate of this value is[27]

$$R = \frac{12\eta L}{1 - 0.63(h/w)}\frac{1}{h^3 w} \quad (1)$$

where $h$, $w$, and $L$ are the height, width, and length of the channel, respectively, and $\eta$ is the dynamic viscosity of water. The total flow rate is divided between the micro- and nanochannels in an inverse proportion to their hydraulic resistances such that


https://dx.doi.org/10.1021/acs.analchem.9b05396
Anal. Chem. 2020, 92, 2847−2852

$$Q_{nano} = Q\frac{R_{total}}{R_{nano}} \approx Q\frac{R_{micro}/2}{R_{nano}} \quad (2)$$

For the channel geometries employed here, the maximum velocity in the nanochannel is about 1000 $\mu$m/s, which corresponds to Reynolds number $10^{-4}$. Hence, even for our highest operational velocities, the flow remains laminar.

**Chemicals.** All further chemicals were purchased from Sigma-Aldrich and solutions were prepared with Milli-Q water with a resistivity of 18.2 Ω cm. We used aqueous solution of 1 mm $Fc(MeOH)_2$ and 0.1 M KCl as supporting electrolyte. $Fc(MeOH)_2$ was selected as a near-ideal reversible, outer sphere redox couple so as to concentrate on mass transport. $Fc(MeOH)_2$ in its reduced form is a neutral species. Slight partial oxidation is however possible due to acid left over in the microfluidic system.[28]

**Measurement protocol.** Prior to measurements, the electrodes were cleaned with $H_2SO_4$ until the cyclic voltammetry pattern became reproducible and corresponded to the characteristic voltammogram expected for clean Pt. The two electrodes were first appointed the roles of generator and collector and a constant pump rate was applied. Initially, both generator and collector were at highly reducing overpotentials (0 V vs Ag/AgCl) and any residual currents were considered as baseline. We then applied a potential step to the generator electrode to an highly oxidizing overpotential (0.5 V vs Ag/AgCl) and measured both the oxidation current at this electrode (generator current) and the reduction current at the second electrode (collector current). The steady-state values of these currents during the potential step period and following baseline subtraction yielded the reported generator and collector currents. The pump rate was then switched to the next flow rate. After completing a set of measurements, the inlet and outlet were swapped and the measurements were repeated for the same range of flow rates. The role of each electrode as generator or collector remained the same, however the upstream electrode became downstream and vice versa. The corresponding results are represented as negative flow velocities.

## RESULTS AND DISCUSSION

**Collector Current.** Figure 3 shows amperometric data measured at the collector elecrode upon applying a square potential pulse of 120 s duration to the generator electrode. The negative sign of the current corresponds to the reduction of species that were earlier oxidized at the generator electrode. After a short transient, the collector current settled to a steady-state plateau value. The magnitude of the current increased with increasing flow rate when the collector was located downstream of the generator, while the opposite trend was observed when the collector was located upstream of the generator.

Figure 4 shows the collector current as a function of flow rate for devices with electrode spacings of 2 $\mu$m, 5 and 50 $\mu$m. For an upstream collector electrode (negative velocity) the current was suppressed at high flow speeds, while at sufficiently high positive flow rates the collector current became approximately linear with flow speed. The transition between these two regimes became increasingly sharp with increasing spacing between the two electrodes, while the collector current at low flow rates increased with decreasing electrode spacing.

This behavior results from two factors. With increasing flow rate, mass transport to the generator is enhanced and the generation rate increases. When the collector is located downstream, advection and diffusion work in tandem and this translates into an increased collection rate. When the collector is located upstream, on the other hand, only diffusion contributes to bringing oxidized molecules to the collector. At high enough flow rates convection dominates and the current to the collector diminishes. Finally, at low flow rates the dominant form of transport between the two electrodes is diffusion. Counterpropagating gradients of oxidized and reduced species are then created (so-called redox cycling). Smaller electrode spacings lead to steeper concentration gradients and hence to larger collector currents.

This intuitive interpretation can be formalized using the Nernst−Planck equation for mass transport. Since the Graetz number Gz ≪ 1, the distribution of species in the transverse directions is essentially independent of the flow rate and we

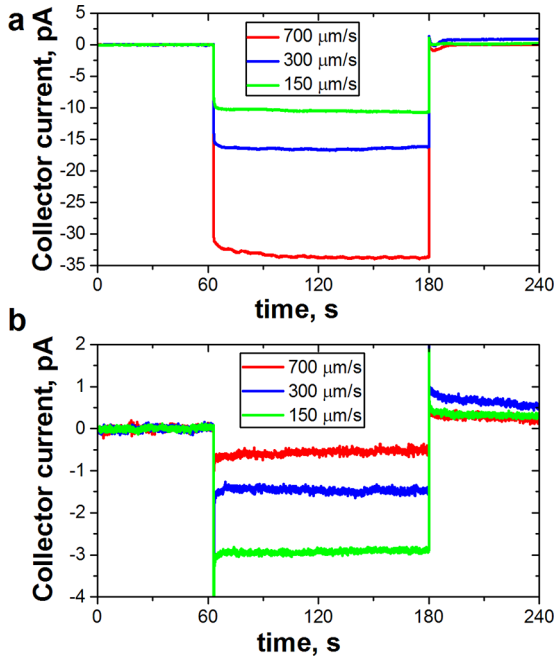


**Figure 3.** Amperometric traces for the reduction current at the collector for several flow velocities when the generator was located (a) upstream and (b) downstream of the collector. This device had a spacing between the electrodes of $s$ = 5 $\mu$m.

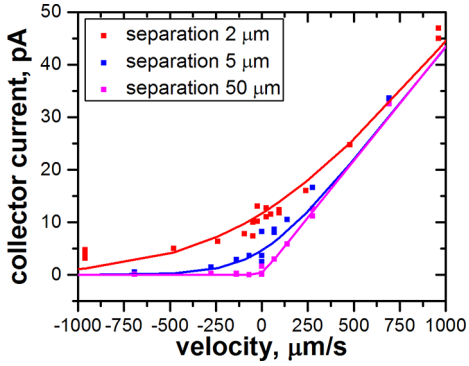


**Figure 4.** Collector currents versus flow rate. Experimental data (symbols) and solutions to the Nernst−Planck equation (solid lines). Positive and negative velocities correspond to the collector being located downstream and upstream from the generator, respectively.


https://dx.doi.org/10.1021/acs.analchem.9b05396
Anal. Chem. 2020, 92, 2847−2852

can describe the longitudinal flux using the one-dimensional Nernst–Planck equation in the steady state,

$$J^{ox} = -D^{ox}\frac{dc^{ox}(x)}{dx} + vc^{ox}(x) \quad (3)$$

where by mass conservation

$$\frac{dJ^{ox}}{dx} = 0 \quad (4)$$

Here the index "ox" indicates that we refer to the oxidized form and $c^{ox}(x)$ is the local concentration of oxidized molecules. The value for the diffusion coefficient of oxidized $Fc(MeOH)_2$, $D^{ox}$, is taken as $5.4 \times 10^{-10}$ $m^2/s$.[29]

Due to the extremely low Graetz number, molecules interact with an electrode as soon as they reach its longitudinal position along the channel. All molecules entering the volume above the generator electrode are thus oxidized, and they are turned back into the reduced form when they reach the boundary of the collector electrode:

$$c^{ox}|_{x=-s/2} = c_b \quad c^{ox}|_{x=s/2} = 0$$

Here $c_b$ is bulk concentration of redox species and $x$ is the position measured from the center of the channel. The solution is easily obtained analytically as

$$c^{ox} = \frac{c_b}{1 - e^{-vs/D^{ox}}} - \frac{c_b\, e^{vx/D^{ox}}}{e^{vs/2D^{ox}} - e^{-vs/2D^{ox}}} \quad (5)$$

as can be verified by direct substitution into eq 3 and eq 4. Calculated concentration profiles for different flow rates are shown in Figure 5.

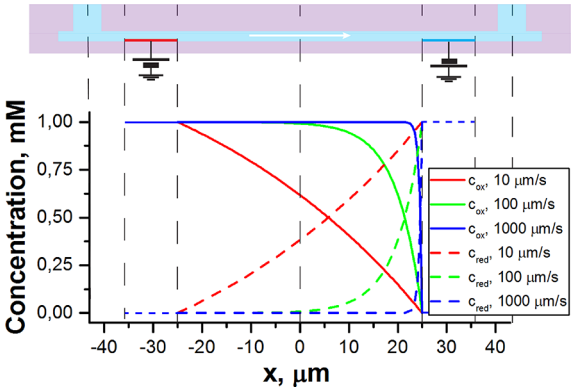


**Figure 5.** Calculated concentration distribution of oxidized species in the space between the generator and collector electrodes for different flow rates. This shows the qualitative difference between the diffusion-limited regime ($Pe^l \ll 1$, red) and convection-limited regime ($Pe^l \gg 1$, blue).

The concentration profile of eq 5 corresponds to a flux of oxidized species at the collector

$$J_{col} = \frac{c_b v}{1 - e^{-vs/D^{ox}}} = \frac{c_b v}{1 - e^{-Pe^l}} \quad (6)$$

and a current

$$i_{col} = nFAJ_{col} = nFAc_b\frac{D}{s}\frac{Pe^l}{1 - e^{-Pe^l}} \quad (7)$$

Here $n = 1$ is the number of electrons transferred per oxidation or reduction event, $F$ is the Faraday constant, and $A$ is the cross-sectional area of the nanochannel.

The predicted trends are consistent with the experimental data of Figure 4. In the regime $Pe^l \ll 1$, corresponding to low flow rates, mass transport is dominated by diffusion and the current is inversely proportional to the spacing between the electrodes:

$$i_{col} \approx nFAc_b\frac{D}{s}$$

This corresponds to a diffusion-limited redox cycling current. In the convection-dominated regime $Pe^l \gg 1$, the collector current at the downstream electrode is controlled primarily by the bulk concentration and the flow velocity:

$$i_{col} \approx nFAc_b v$$

Finally, for the collector current at the upstream electrode and a large negative value of $Pe^l$, the current is exponentially suppressed and we have

$$i_{col} \approx 0$$

Theoretical curves based on eq 7 are shown in Figure 4. The crossover value of $Pe^l = 1$ is reached for electrode spacings 2, 5, and 50 $\mu$m at velocities of 270, 180, and 18 $\mu$m/s, respectively. Consistent with the experiment, the current near zero fluid velocity scales as $1/s$ and at high velocities the dependence on velocity becomes linear.

Some scatter in the experimental data is however observed. We attribute this mainly to uncertainties in the flow velocity, which is highly sensitive to the dimensions of nano- and microchannels. While our mathematical model considers these to have a constant and well-defined shape and size, they may differ slightly due to inaccuracies in the fabrication process and deformation of the PDMS channels over the course of the experiments. For example, it was shown previously[30,31] that at high flow rates the actual velocity can be 30% smaller than the calculated value. Small PDMS particles can also get into the microchannel during measurements and temporally alter the flow velocity.

Within the accuracy imposed by this scatter, the good agreement between theory and experiment allows concluding that mass transport is well described by the Nernst–Planck equation (eq 3). This supports the assumption that the faradaic current is dominated by mass transport in solution and that surface transport of adsorbed redox species has at most a marginal effect on the total current.

**Generator Current.** Figure 6 shows the steady-state generator current as a function of average fluid velocity and electrode separation. The generator current is largely symmetric around $v = 0$ and increases with increasing flow speed.

As illustrated in Figure 7, the generator electrode collects reduced species from two sources: the collector electrode and the inlet or outlet of the nanochannel. It is a good approximation to consider these two fluxes separately as they are directed to the generator electrode from two opposite directions. Each flux can be independently estimated from the one-dimensional Nernst–Planck equation. Here, however, we use the value of the diffusion coefficient for the reduced form of $Fc(MeOH)_2$, $D^{red} = 6.7 \times 10^{-10}$ $m^2/s$:[29]


https://dx.doi.org/10.1021/acs.analchem.9b05396
Anal. Chem. 2020, 92, 2847–2852

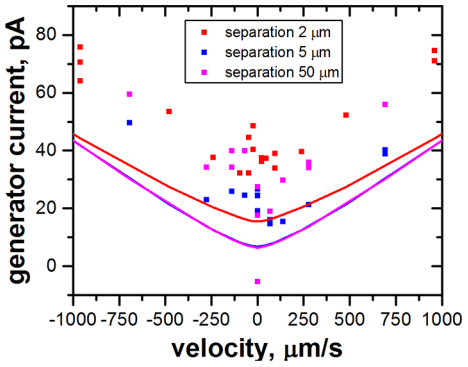


**Figure 6.** Generator currents. Experimental data (scatter) and solution of Nernst–Planck equation (solid lines).


**Figure 7.** Fluxes of reduced molecules to the generator electrode: $J_1$ from the bulk solution outside the nanogap device and $J_2$ from the collector electrode via redox cycling.

$$J_{1,\mathrm{gen}} = -D^{\mathrm{red}} \frac{\mathrm{d}c^{\mathrm{red}}}{\mathrm{d}x} + vc_{\mathrm{red}}$$

$$J_{2,\mathrm{gen}} = -D^{\mathrm{red}} \frac{\mathrm{d}c^{\mathrm{red}}}{\mathrm{d}x} - vc_{\mathrm{red}} \quad (8)$$

The boundary conditions are also analogous:

$$c^{\mathrm{red}}|_{x_1=0} = c_{\mathrm{b}} \quad c^{\mathrm{red}}|_{x_1=l_{\mathrm{access}}} = 0$$

$$c^{\mathrm{red}}|_{x_2=0} = 0 \quad c^{\mathrm{red}}|_{x_2=s} = c_{\mathrm{b}}$$

Here $l_{\mathrm{access}}$ is the distance between the inlet/outlet and the generator electrode, $x_1$ refers to the position between the inlet/outlet and the generator electrode, and $x_2$ to the position between the two electrodes. The solution yields for the current

$$i_{\mathrm{gen}} = nFA(J_{1,\mathrm{gen}} + J_{2,\mathrm{gen}})$$

$$= nFAc_{\mathrm{b}}v\left(\frac{1}{1 - \mathrm{e}^{-vl_{\mathrm{access}}/D^{\mathrm{red}}}} - \frac{1}{1 - \mathrm{e}^{vs/D^{\mathrm{red}}}}\right) \quad (9)$$

This expression is expressed in terms of $v$ rather than $Pe^{\mathrm{l}}$ to avoid confusion since the two contributions have different values of $Pe^{\mathrm{l}}$.

The predictions of eq 9 are compared to the experimental data in Figure 6. The theoretical curves capture the experimental trend, but the actual values have a systematic offset of ~+20 pA. As discussed in the Supporting Information, this error is attributed to leakage through the passivation layer protecting the wires connecting the electrodes to outer contact pads. This leakage did not affect the reduction current at the collector electrode as oxidized molecules are produced inside the nanochannel at the generator electrode.

## CONCLUSION

We examined mass transport in nanochannels in a generator-collector configuration both experimentally and theoretically. The low $Gz$ number allowed us to use an effective 1D model for the mathematical description of this system, and the experimental results correspond well with the calculated curves. Closely spaced electrodes can exhibit significant cross-talk by means of diffusion, while for sufficiently distant electrodes only convection is relevant.

## ASSOCIATED CONTENT

### Supporting Information

The Supporting Information is available free of charge at https://pubs.acs.org/doi/10.1021/acs.analchem.9b05396.

Discussion of leakage current for the generator electrode (PDF)

## AUTHOR INFORMATION

### Corresponding Author

**Serge G. Lemay** − *MESA+ Institute for Nanotechnology and Faculty of Science and Technology, University of Twente 7500 AE Enschede, The Netherlands;* orcid.org/0000-0002-0404-3169; Email: s.g.lemay@utwente.nl

### Author

**Zinaida A. Kostiuchenko** − *MESA+ Institute for Nanotechnology and Faculty of Science and Technology, University of Twente 7500 AE Enschede, The Netherlands*

Complete contact information is available at: https://pubs.acs.org/10.1021/acs.analchem.9b05396

### Notes

The authors declare no competing financial interest.

## ACKNOWLEDGMENTS

This work was supported financially in part by the European Research Council (ERC) under Project 278801.

## REFERENCES

(1) Frumkin, A.; Nekrasov, L.; Levich, B.; Ivanov, J. *J. Electroanal. Chem. (1959-1966)* **1959**, *1*, 84–90.
(2) Gerischer, H.; Mattes, I.; Braun, R. *J. Electroanal. Chem. (1959-1966)* **1965**, *10*, 553–567.
(3) Itagaki, M.; Suzuki, T.; Watanabe, K. *Electrochim. Acta* **1997**, *42*, 1081–1086.
(4) Tsuru, T. *Mater. Sci. Eng., A* **1991**, *146*, 1–14.
(5) Sasaki, H.; Maeda, M. *J. Electrochem. Soc.* **2010**, *157*, C414–C418.
(6) Shrestha, B. R.; Yadav, A. P.; Nishikata, A.; Tsuru, T. *Electrochim. Acta* **2011**, *56*, 9714–9720.
(7) Unwin, P. R. *J. Electroanal. Chem. Interfacial Electrochem.* **1991**, *297*, 103–124.
(8) Oltra, R.; Indrianjafy, G.; Keddam, M.; Takenouti, H. *Corros. Sci.* **1993**, *35*, 827–832.
(9) Heller-Ling, N.; Poillerat, G.; Koenig, J.; Gautier, J.; Chartier, P. *Electrochim. Acta* **1994**, *39*, 1669–1674.
(10) Zhao, M.; Hibbert, D. B.; Gooding, J. J. *Anal. Chem.* **2003**, *75*, 593–600.
(11) Paixao, T. R. L. C.; Richter, E. M.; Brito-Neto, J. G. A.; Bertotti, M. *J. Electroanal. Chem.* **2006**, *596*, 101–108.
(12) Renault, C.; Anderson, M. J.; Crooks, R. M. *J. Am. Chem. Soc.* **2014**, *136*, 4616–4623.
(13) Anderson, M. J.; Crooks, R. M. *Anal. Chem.* **2014**, *86*, 9962–9969.
(14) Wu, J.; Sansen, W. *Sens. Actuators, A* **2002**, *97–98*, 68–74.
(15) Amatore, C.; Belotti, M.; Chen, Y.; Roy, E.; Sella, C.; Thouin, L. *J. Electroanal. Chem.* **2004**, *573*, 333–343.
(16) Wu, J.; Ye, J. *Lab Chip* **2005**, *5*, 1344–1347.
(17) Kjeang, E.; Roesch, B.; McKechnie, J.; Harrington, D. A.; Djilali, N.; Sinton, D. *Microfluid. Nanofluid.* **2007**, *3*, 403–416.

(18) Amatore, C.; Da Mota, N.; Lemmer, C.; Pebay, C.; Sella, C.; Thouin, L. *Anal. Chem.* **2008**, *80*, 9483−9490.
(19) Braun, R. *J. Electroanal. Chem. Interfacial Electrochem.* **1968**, *19*, 23−35.
(20) Tokuda, K.; Matsuda, H. *J. Electroanal. Chem. Interfacial Electrochem.* **1974**, *52*, 421−431.
(21) Compton, R. G.; Stearn, G. M. *J. Chem. Soc., Faraday Trans. 1* **1988**, *84*, 4359−4367.
(22) Compton, R. G.; Coles, B. A.; Fisher, A. C. *J. Phys. Chem.* **1994**, *98*, 2441−2445.
(23) Alden, J. A.; Compton, R. G. *J. Electroanal. Chem.* **1996**, *415*, 1−12.
(24) Cooper, J. A.; Compton, R. G. *Electroanalysis* **1998**, *10*, 141−155.
(25) Thompson, M.; Klymenko, O. V.; Compton, R. G. *J. Electroanal. Chem.* **2005**, *576*, 333−338.
(26) Kang, S.; Mathwig, K.; Lemay, S. G. *Lab Chip* **2012**, *12*, 1262−1267.
(27) Bruus, H. *Lab Chip* **2011**, *11*, 3742−3751.
(28) Sarkar, S. *Unconventional Electrochemistry in Nanogap Transducers*. Ph.D. Thesis, University of Twente, Enschede, The Netherlands, 2016.
(29) Martin, R. D.; Unwin, P. R. *Anal. Chem.* **1998**, *70*, 276−284.
(30) Mathwig, K.; Lemay, S. G. *Micromachines* **2013**, *4*, 138−148.
(31) Mathwig, K.; Mampallil, D.; Kang, S.; Lemay, S. G. *Phys. Rev. Lett.* **2012**, *109*, 118302.


https://dx.doi.org/10.1021/acs.analchem.9b05396
*Anal. Chem.* 2020, 92, 2847−2852